Tidal Estimation in the Atlantic and Indian Oceans

Braulio V. Sanchez

Laboratory for Terrestrial Physics
Goddard Space Flight Center
Greenbelt, Maryland

Desiraju B. Rao

National Metereological Center
National Oceanic and Atmospheric Administration
Washington, D.C.

Stephen D. Steenrod

Applied Research Corporation
Landover, Maryland

Abstract   An estimation technique has been developed to extrapolate tidal amplitudes and phases over entire ocean basins using existing gauge data and the altimetric measurements which are now beginning to be provided by satellite oceanography. The technique was tested previously in the Lake Superior basin by Sanchez et al. (1985). The method has now been developed and applied in the Atlantic-Indian ocean basins using a $6° \times 6°$ grid to test its essential features.

The functions used in the interpolation are the eigenfunctions of the velocity potential (Proudman functions), which are computed numerically from a knowledge of the basin's bottom topography, the horizontal plan form, and the necessary boundary

conditions. These functions are characteristic of the particular basin.

The gravitational normal modes of the basin, computed as part of the investigation, are used to obtain the theoretical forced solutions for the tidal constituents. The latter provide the simulated data for testing of the method and serve as a guide in choosing the most energetic functions for the interpolation. The results of the estimation of the M_2 and K_1 tidal constituents indicate the possibility of recovering the tidal signal with a degree of accuracy well within the error bounds of present satellite techniques.

Introduction

The accurate modeling of oceanic tides is very important for the interpretation of oceanic measurements from spaceborne altimeters. The tides not only introduce errors into the determination of geostrophic velocity but are of considerable interest in their own right. Tidal investigations of ocean basins with realistic topography and coastal boundaries are still in the development stage.

Ocean tidal studies have a long history. Several comprehensive reviews can be found in the literature (i.e., Hendershott and Munk, 1970; Cartwright, 1977; Hendershott, 1973, 1977, 1981; Schwiderski, 1980). Hendershott (1977) summarized the efforts to solve the Laplace tidal equations (LTEs) for global tides for semidiurnal and diurnal components up to that time.

More recent efforts have been directed to incorporate the results of loading and self-attraction. Accad and Pekeris (1978) solve the LTEs for the M_2 and S_2 tides in the world oceans on the basis of a knowledge of the tidal potential alone. Tidal dissipation was taken to be limited to the coastline. The main purpose of their investigation was to determine the effects of tidal self-attraction and of tidal loading. An iterative method was developed to evaluate these secondary effects. The resulting change is of the order of 10% and better agreement is obtained between the theoretical and observed tides. Parke and Hendershott (1980) obtained global solutions to the LTEs for the M_2, S_2, and K_1 tides. They addressed the problem of divergence of the near-resonance modes by means of test functions which are used to interpolate between island data

in the least-squares sense. These test functions are derived by solving the LTEs with ocean loading and self-gravitation in an iterative manner. The resulting representations of the global tide are stable over at least a $\pm 5\%$ variation in the mean depth of the model basin and they conserve mass.

Schwiderski (1980) computed the M_2 global tide by solving the LTEs directly, using a finite difference scheme in space and time; the strictly mathematical solution was modified by means of an interpolation technique which incorporates over 2000 tide data collected at continental and island stations. The interpolation is accomplished by adjusting the bottom friction coefficient and by allowing inflow or outflow across the mathematical ocean boundary. No direct comparison of observed and computed data is feasible since the model incorporates essentially all known data, although it is possible to evaluate the smoothness with which the computed tide accepts or rejects data. It was found that the interpolation technique permits a check of the reality of both the tide model and the tidal data input.

Platzman (1978, 1981, 1984) has computed a range of normal modes for the world oceans. He used them to synthesize some of the diurnal and semidiurnal tides. He decomposed the transport vector by means of the Stokes/Helmholtz potentials but did not determine the velocity potential and stream function eigenfunctions explicitly (as in this paper), but proceeded directly to the normal-mode solution of the LTEs. The linearized primitive equations were discretized by means of first-order, piecewise-linear finite elements with an average grid triangle area equal to that of a 4.54° equatorial square. His synthesized tides incorporated dissipation by means of energy flux across the domain boundary, and no tidal loading or self-attraction was included.

Simulation studies by Estes (1980) using numerical solutions of the LTEs to generate the observed measurements (based on simulated 4-day SEASAT orbits over a 200-day interval) indicate that when the rms amplitude error is less than 10 cm for the M_2 tide, virtually all the structure is recovered. For rms errors between 12 and 15 cm, all large-scale features are retained; for 15- to 20-cm rms errors, the high-amplitude structure is recovered. These results were obtained by utilizing long arc intersection or crossover point

data and simultaneously solving for the orbit error parameters with the tide model parameters.

Mazzega (1985) created a global model of the M_2 tide using 24 days of SEASAT altimetry data. The solution was obtained by means of surface spherical harmonics, and the results were qualitatively realistic. No hydrodynamic equations were used.

Woodworth and Cartwright (1986) have extracted the M_2 ocean tide from SEASAT altimetry data. They used three complementary methods. The first method provides point measurements of the tide at the crossovers of the SEASAT repeat orbit ground track; it was applied in the tropical ocean areas. The other two methods involve the spatial expansion of M_2 in terms of surface spherical harmonics or Platzman normal modes of the world ocean. The results reproduce many features of the tide represented in recent tidal models.

The purpose of this investigation is to develop an estimation technique which will serve to extrapolate tidal amplitudes and phases over entire ocean basins using existing gauge data and the precise altimetric measurements which are now beginning to be provided by satellite oceanography. The applicability of the extrapolating technique was tested in the Lake Superior basin by Sanchez et al. (1985). Proceeding in stages we now report the results obtained in the Atlantic and Indian Oceans using a $6° \times 6°$ grid. At this level of resolution it is possible to test the essential features of the method without using real data.

The method to be used in this investigation requires several distinct steps. First it is necessary to determine numerically the stream function and velocity potential orthogonal functions (the Stokes/Helmholtz potentials) which span the space of the basin under consideration. These space functions are then used in the LTEs to determine the homogeneous solution (normal modes) and the forced solution. The latter is obtained by adding the astronomical forcing function modified to include solid-earth tides.

The velocity potential eigenfunctions obtained as a first step are also used to extrapolate the surface height field over the entire space domain of the given basin, and this approach will constitute a distinct and integral part of the investigation. The theoretical foundation is Proudman's theory (1918) as formulated by Rao (1966). The theory provides the formalism for calculation of the gravitational (first-class) normal modes and the rotational (second-

class or Rossby waves) normal models of irregularly shaped basins with realistic bathymetry.

The method requires the solution of two elliptic partial differential equations with second-order operators which are simpler than the tidal operator. The boundary conditions correspond to vanishing of the stream function and normal derivative of the velocity potential. The elliptic operators are represented numerically in finite difference form; the grid used is a Richardson lattice which preserves self-adjointness. The solutions yield the velocity and surface height fields in terms of orthogonal functions with time-dependent coefficients. These functions are then substituted into the LTEs: If the homogeneous equations are used, one obtains the normal modes; if the forcing terms are included, the forced solution is obtained. In both cases the solution is obtained numerically. The surface height field is dependent only on the velocity potential orthogonal functions. The expansion coefficients of these functions can be estimated in a least-squares sense from available selected tidal measurements.

Basic Equations

Free Solutions

The method of approach was originally developed by Proudman (1918) using a Lagrangian approach. It was reformulated by Rao (1966) from the Eulerian point of view. The basic ideas of the method presented below follow Rao's line of development. The basic equations are the linearized shallow water equations on a rotating plane:

$$\frac{\partial \mathbf{M}}{\partial t} - f[\mathbf{M}] = -g\bar{H}h\nabla\eta$$
$$\frac{\partial \eta}{\partial t} + \nabla \cdot \mathbf{M} = 0 \tag{1}$$

where

$$\mathbf{M} \equiv H\mathbf{V} \equiv (M, N)$$
$$\mathbf{V} \equiv (u, v)$$
$$f \equiv 2\omega \sin \theta$$
$$h(x, y) \equiv H(x, y)/\bar{H}$$

$H(x, y)$ is the variable depth of the fluid in equilibrium, $\bar{H}$ some constant scaling depth, f the Coriolis parameter, $\mathbf{V}$ the horizontal velocity vector, η the fluctuation of the free surface, g the apparent gravitational acceleration, and ∇ the horizontal gradient operator. Brackets denote rotation of the vector through a right angle in the clockwise direction of the horizontal plane (i.e., $[\ ] = -(\mathbf{k} \times \nabla)$, $\mathbf{k}$ being a unit vector vertical to the horizontal plane).

The appropriate boundary conditions to be adjoined to equation (1) are

$$\mathbf{M} \cdot \mathbf{n} = 0 \tag{2}$$

on the coast, where $\mathbf{n}$ is the unit normal to the coastline. The transport vector $\mathbf{M}$ may be partitioned as follows:

$$\mathbf{M} = \mathbf{M}^\phi + \mathbf{M}^\psi \tag{3}$$

where

$$\begin{aligned}\mathbf{M}^\phi &= -h\nabla\phi \\ \mathbf{M}^\psi &= -[\nabla\psi]\end{aligned} \tag{4}$$

$\mathbf{M}^\psi$ is the solenoidal part of $\mathbf{M}$ and $h^{-1}\mathbf{M}^\phi$ is the irrotational part since

$$\begin{aligned}\nabla \cdot [h^{-1}\mathbf{M}^\phi] &= 0 \\ \nabla \cdot \mathbf{M}^\psi &= 0\end{aligned}$$

To complete the determination of ϕ and ψ, it is necessary to specify the boundary conditions $\mathbf{M}^\phi \cdot \mathbf{n} = 0$ and $M^\psi \cdot \mathbf{n} = 0$ to ensure that equation (2) is satisfied. In terms of ϕ and ψ, then, the conditions are

and

$$\begin{aligned}h\frac{\partial\phi}{\partial n} &= 0 \\ \psi &= 0\end{aligned} \tag{5}$$

on the boundaries.

The divergence of the transport field and the vorticity of the velocity field yield

$$\begin{aligned}\nabla \cdot \mathbf{M} &= -\nabla \cdot h\nabla\phi \\ \nabla \cdot [h^{-1}\mathbf{M}] &= \nabla \cdot h^{-1}\nabla\psi\end{aligned} \tag{6}$$

If $\mathbf{M}$ is known as a function of the horizontal coordinates, the left sides of equations (6) are specified. Then each equation represents an inhomogeneous elliptic differential equation with homogeneous boundary conditions given by equations (5), and it is well known that such problems possess a unique solution. It is also straightforward to prove that the representation of $\mathbf{M}$ as given in equations (3) through (5) is unique. Since $\mathbf{M}$ itself is unknown, the procedure then consists of expanding ϕ and ψ in terms of the spectra of the elliptic operators appearing in equations (6); that is, we seek solutions that satisfy the equations

$$\begin{aligned}\nabla \cdot h\nabla\phi_\gamma &= -\lambda_\gamma\phi_\gamma \\ \nabla \cdot h^{-1}\nabla\psi_\gamma &= -\mu_\gamma\psi_\gamma\end{aligned} \tag{7}$$

where ϕ_γ and ψ_γ are the characteristic functions and λ_γ and μ_γ are the characteristic values associated with the corresponding operators $\nabla \cdot h\nabla$ and $\nabla \cdot h^{-1}\nabla$. The characteristic functions satisfy the boundary conditions

$$\begin{aligned}h\frac{\partial\phi_\gamma}{\partial n} &= 0 \\ h^{-1}\psi_\gamma &= 0\end{aligned} \tag{8}$$

The condition $h^{-1}\psi_\gamma = 0$ imposes a stronger condition than that required by equations (5). However, the factor h^{-1} is necessary to make the ψ_γ problem self-adjoint. Since the problems (7) and (8) are self-adjoint, the characteristic values λ_γ and μ_γ are real and the characteristic functions ϕ_γ and ψ_γ each constitute a complete and internally orthogonal set. Without loss of generality, the orthogonality condition may be chosen as

$$\begin{aligned}\int h^{-1}\mathbf{M}_\gamma^\phi \cdot \mathbf{M}_\beta^\phi \, dA &= \lambda_\gamma \int \phi_\gamma\phi_\beta \, dA = Ac^2\bar{H}^2\delta_{\gamma\beta} \\ \int h^{-1}\mathbf{M}_\gamma^\psi \cdot \mathbf{M}_\beta^\psi \, dA &= \mu_\gamma \int \psi_\gamma\psi_\beta \, dA = Ac^2\bar{H}^2\delta_{\gamma\beta}\end{aligned} \tag{9}$$

where $c^2 = gH$ and A is the surface area of the basin; $\delta_{\gamma\beta}$ is the Kronecker delta. We have further defined, in accordance with equation (4),

$$\mathbf{M}_\gamma^\phi = -h\nabla\phi_\gamma \quad \text{and} \quad \mathbf{M}_\gamma^\psi = -[\nabla\psi_\gamma]$$

in the orthogonality condition (9).

The components of the transport vector can now be represented by the sums

$$\mathbf{M}^\phi = \sum_\gamma P_\gamma \mathbf{M}_\gamma^\phi$$
$$\mathbf{M}^\psi = \sum_\gamma Q_\gamma \mathbf{M}_\gamma^\psi \qquad (10)$$

where P_γ and Q_γ are the expansion coefficients. The orthogonality conditions ensure that equations (10) represent the least-squares approximations to $\mathbf{M}^\phi$ and $\mathbf{M}^\psi$ if and when the sums span the complete spectra of equations (7). The height field η is governed by the divergent part of $\mathbf{M}$, and the ϕ_γ functions yield a sufficient basis for its representation. A convenient representation for η may be taken as

$$\eta = \sum_\gamma R_\gamma \eta_\gamma$$
$$\eta_\gamma = c^{-1}(\lambda_\gamma)^{1/2}\phi_\gamma \qquad (11)$$

where R_γ are the expansion coefficients for the η-field.

Substitution of equations (10) and (11) into equations (1) and use of the orthogonality conditions (9) yield a set of prediction equations for the expansion coefficients:

$$\frac{dP}{dt}\gamma - \sum_\beta A_{\gamma\beta}P_\beta - \sum_\beta B_{\gamma\beta}Q_\beta - v_\gamma R_\gamma = 0$$
$$\frac{dQ}{dt}\gamma - \sum_\beta C_{\gamma\beta}P_\beta - \sum_\beta D_{\gamma\beta}Q_\beta = 0 \qquad (12)$$
$$\frac{dR}{dt}\gamma + v_\gamma P_\gamma = 0$$

where the coupling coefficients are given by

$$A_{\gamma\beta} \equiv \{\mathbf{M}_\gamma^\phi, [\mathbf{M}_\beta^\phi]\} \qquad B_{\gamma\beta} \equiv \{\mathbf{M}_\gamma^\phi, [\mathbf{M}_\beta^\psi]\}$$
$$C_{\gamma\beta} \equiv \{\mathbf{M}_\gamma^\psi, [\mathbf{M}_\beta^\phi]\} \qquad D_{\gamma\beta} \equiv \{\mathbf{M}_\gamma^\psi, [\mathbf{M}_\beta^\psi]\} \qquad (13)$$

The quantity inside the braces represents an inner product of two vectors $\mathbf{W}$ and $\mathbf{T}$ and is denoted by

$$\{\mathbf{W}, \mathbf{T}\} = (1/c^2 A\bar{H}^2)\int_A fh^{-1}\mathbf{W}\cdot\mathbf{T}\,dA$$

It can be seen from equations (12) and (13) and the definition of the inner product that all the coupling coefficients vanish when the Coriolis parameter $f = 0$ and hence

$$\frac{d^2 P_\gamma}{dt^2} + v_\gamma^2 P_\gamma = 0$$

$v_\gamma = (c^2\lambda_\gamma)^{1/2}$ is the nonrotating frequency of oscillation. In equations (12) and (13) the subscript γ (or β) is used as a proxy for a binary index and represents an ordering of the characteristic functions ϕ_γ, ψ_γ in some as yet unspecified manner. For convenience we replace the wavenumber index γ by scalar indices $i = 1, 2, 3$ (or $j = 1, 2, 3, \dots$) and denote

$$\begin{array}{ccc} \lambda_i \equiv \lambda_{\gamma i} & M_i \equiv M_{\gamma i} & v_i \equiv v_{\gamma i} \\ P_i \equiv P_{\gamma i} & Q_i \equiv Q_{\gamma i} & R_i \equiv R_{\gamma i} \\ & A_{ij} \equiv A_{\gamma i \beta j} & \\ & B_{ij} \equiv B_{\gamma i \beta j} & \\ & C_{ij} \equiv C_{\gamma i \beta j} & \\ & D_{ij} \equiv D_{\gamma i \beta j} & \end{array} \qquad (14)$$

Using the notation above, we can define column vectors

$$\mathbf{P} \equiv \mathrm{col}\,(P_i), \qquad \mathbf{Q} = \mathrm{col}\,(Q_i), \qquad \mathbf{R} = \mathrm{col}\,(R_i)$$
$$S \equiv \begin{vmatrix} \mathbf{P} \\ \mathbf{Q} \\ \mathbf{R} \end{vmatrix} \qquad (15a)$$

and matrices

$$A \equiv \{A_{ij}\} \qquad B \equiv \{B_{ij}\}$$
$$C \equiv \{C_{ij}\} \qquad D \equiv \{D_{ij}\} \qquad (15b)$$
$$\langle v \rangle \equiv \text{diagonal } v_i$$

Equations (12) may now be written in the form

$$\frac{d\mathbf{s}}{dt} + a\mathbf{S} = 0 \qquad (16)$$

where a is the square matrix

$$a \equiv \begin{vmatrix} -A & -B & -\langle v \rangle \\ -C & -D & 0 \\ \langle v \rangle & 0 & 0 \end{vmatrix} \qquad (17)$$

In seeking the solutions for the normal modes, we assume that

$$\mathbf{S} \sim e^{i\sigma t}$$

where σ is the normal-mode frequency with rotation and $i \equiv \sqrt{-1}$. Equation (15) then reduces to

$$(\sigma \text{II} - ia)\mathbf{S} = 0 \qquad (18)$$

In equation (18), II is the identity matrix and the σ's are the characteristic values of the matrix ia. From the definition of the coupling coefficients given in equation (13) and the matrix a as defined in equation (17), it is clear that ia exhibits Hermitian symmetry and hence the σ's constitute a spectrum of real eigenvalues. In computing the matrix elements in a, the basis functions ϕ_i and ψ_i are chosen to correspond to an ordering of the characteristic values λ_i and μ_i arranged so that $\lambda_1 < \lambda_2 < \lambda_3 \cdots$ and $\mu_1 < \mu_2 < \mu_3 \cdots$. Such an ordering has been chosen since the λ_i's and μ_i's have the dimensions of (wavenumber)^2. Hence, at any order of truncation, those ϕ_i's and ψ_i's with the largest space scales are taken into account.

Forced Solution

In the computation of the forced solution we include the effects of the yielding of the solid earth to tide-generating forces. The effects due to self-attraction of the tide and tidal loading as well as the frictional effects have not been included. The theory allows for the inclusion of these effects, but they introduce computational complications and physical uncertainties and they are not necessary in the context of the application of the interpolation technique. Equa-

tions (1) are recast for the forced tidal oscillations as

$$\frac{\partial \mathbf{M}}{\partial t} - f[\mathbf{M}] = -g\bar{H}h\nabla\eta' $$
$$\frac{\partial \eta}{\partial t} + \nabla \cdot \mathbf{M} = 0 \qquad (19)$$

where

$$\eta' = \eta - (1 + k_2 - h_2)\bar{\eta}$$

k_2 and h_2 are the Love numbers and $\bar{\eta}$ is the equilibrium tide height. Let the vector $\mathbf{G} = g\bar{H}h(1 + k_2 - h_2)\nabla\bar{\eta}$. Equations (19) can then be written

$$\frac{\partial \mathbf{M}}{\partial t} - f[\mathbf{M}] = -g\bar{H}h\nabla\eta + \mathbf{G} $$
$$\frac{\partial \eta}{\partial t} + \nabla \cdot \mathbf{M} = 0 \qquad (20)$$

Substitution of the expansions (10) and (11) into equations (20) yields, after using equation (13),

$$\frac{dP_\gamma}{dt} - \sum_\beta A_{\gamma\beta}P_\beta - \sum_\beta B_{\gamma\beta}Q_\beta - v_\gamma R_\gamma = (c^2 A\bar{H}^2)\int fh^{-1}\mathbf{G} \cdot \mathbf{M}_\gamma^\phi \, dA$$

$$\frac{dQ_\gamma}{dt} - \sum_\beta C_{\gamma\beta}P_\beta - \sum_\beta D_{\gamma\beta}Q_\beta = (c^2 A\bar{H}^2)^{-1}\int fh^{-1}\mathbf{G} \cdot \mathbf{M}_\gamma^\psi \, dA$$

$$\frac{dR_\gamma}{dt} + v_\gamma P_\gamma = 0$$

$$(21)$$

Define the vector $\mathbf{F}$ as follows:

$$\mathbf{F} = \begin{vmatrix} (c^2 A\bar{H}^2)^{-1}\int fh^{-1}\mathbf{G} \cdot \mathbf{M}_\gamma^\phi \, dA \\ (c^2 A\bar{H}^2)^{-1}\int fh^{-1}\mathbf{G} \cdot \mathbf{M}_\gamma^\psi \, dA \\ 0 \end{vmatrix} \qquad (22)$$

Equations (21) can then be written as an inhomogeneous matrix equation

$$\frac{d\mathbf{S}}{dt} + a\mathbf{S} = \mathbf{F} \tag{23}$$

where $\mathbf{S}$ and a are defined by equations (15a) and (17). The solution of equation (23) is given by

$$\mathbf{S} = C\langle e^{i\sigma t}\rangle \int_0^t \langle e^{-i\sigma\tau}\rangle C^{-1}\mathbf{F}(\tau)\,d\tau \tag{24}$$

where C is the modal matrix containing the eigenvectors of a arranged in columns and σ are the characteristics values of a. $\langle e^{i\sigma t}\rangle$ is a diagonal matrix.

Estimation

The orthogonal functions ϕ_γ form a basis for the expansion of the height field η, as discussed earlier. Since these functions are characteristic for a particular basin and are described at all points inside the basin (within the resolution of the finite difference grid), they can be used as optimal functions for extrapolation of the tidal field over the whole basin, given data at some selected points.

Even though the basis functions are orthogonal, in fitting the data to these functions it is preferable to use linear least-squares techniques to determine the coefficients of expansion rather than the orthogonality property since real data are not usually available at regularly spaced points. A similar approach was taken in a previous investigation by Rao and Schwab (1981) in which they determined the steady circulation in a closed basin for which the appropriate orthogonal functions are the ψ_γ functions, and Sanchez et al. (1985) used the ϕ_γ functions for tidal extrapolation in Lake Superior. An outline of the procedure and the basic equations involved are given below.

The tidal height field as given by equations (11) and (15) can be written

$$\eta(x, y, t) = \sum_\gamma R_{\gamma r}\eta_\gamma(x, y)\cos\delta t - \sum_\gamma R_{\gamma I}\eta_\gamma(x, y)\sin\delta t \tag{25}$$

where $R_{\gamma r}$ and $R_{\gamma I}$ denote the real and imaginary parts of R_γ. The tidal height field can also be expressed in terms of amplitude $A(x, y)$ and phase $\Theta(x, y)$, that is,

$$\eta(x, y, t) = A(x, y)\cos[\sigma t - \Theta(x, y)] \tag{26}$$

Comparing equations (25) and (26), one obtains the following relations:

$$A(x, y) = \left[\left(\sum_\gamma R_{\gamma r}\eta_\gamma\right)^2 + \left(\sum_\gamma R_{\gamma I}\eta_\gamma\right)^2\right]^{1/2}$$
$$\Theta(x, y) = \arctan\left[-\left(\sum_\gamma R_{\gamma I}\eta_\gamma\right)\bigg/\left(\sum_\gamma R_{\gamma r}\eta_\gamma\right)\right] \tag{27}$$

Also, from equations (25) and (26) one obtains the following vector-matrix relations:

$$[\eta]\mathbf{R}_r = \mathbf{A}\cos\theta$$
$$[\eta]\mathbf{R}_I = \mathbf{A}\sin\theta \tag{28}$$

The components of the vectors $\mathbf{A}\cos\theta$ and $\mathbf{A}\sin\theta$ are the n available tidal measurements. The matrix $[\eta]$ is available from the solution of the velocity potential eigenfunctions; its k columns will correspond to the velocity potential eigenfunctions chosen to represent the forced solution, and its n rows correspond to the location of the tidal measurements in the basin under consideration. The least-squares solution to equations (28) is then given by

$$\mathbf{R}_r = ([\eta]^T[\eta])^{-1}[\eta]^T\mathbf{A}\cos\theta$$
$$\mathbf{R}_I = ([\eta]^T[\eta])^{-1}[\eta]^T\mathbf{A}\sin\theta \tag{29}$$

where $[\eta]^T$ is the transposed matrix. Having determined a certain number of coefficients $\mathbf{R}_r$ and $\mathbf{R}_I$, since the functions $\eta_\gamma(x, y)$ are known over the entire basin, one can obtain the amplitude and phase of the tidal height at all points in the basin from equation (27). The maximum number of coefficients $\mathbf{R}_r$ and $\mathbf{R}_I$ that can be determined will be the same as the number of observations available.

Results

Normal Modes and Forced Solutions

A normal-mode solution for the Atlantic and Indian Oceans has been obtained by means of a 6° × 6° finite difference grid. There are 462 velocity potential and 370 stream function points distributed such as to form a single Richardson lattice. A finite difference solution of equations (7) subject to the boundary conditions given by equations (8) yields the eigenvalues and eigenvectors for both fields. The eigenfunctions of the ϕ solution represent the nonrotating gravitational normal modes of the basin. The periods of oscillation of the lowest modes are given in the first column of Table 1. The stream function modes generate the vorticity component of the flow field in the rotating case for the gravitational and rotational species. They are more dominant for the quasi-geostrophic rotational modes than for the gravitational modes. The normal-mode solution was obtained by including the lowest 150 eigenfunctions from each field (ϕ and ψ) into the dynamical equations. The solution of the eigenvalue problem posed by equation (18) yields the normal modes. The normal modes fall into two distinct categories: the inertia-gravitational, modified by rotation, and the rotational, modified by divergence. If the secular determinant is truncated at a size $n \times n$, one obtains $2n/3$ gravitational modes and $n/3$ rotational modes, in pairs (plus and minus the same value). In our case there are 300 gravitational modes and 150 rotational modes. The rotational modes are characterized by high ratios of kinetic to potential energy; these modes will vanish in a basin of constant depth and Coriolis parameter. The rotational normal modes are extremely sensitive to the resolution of the shape of the basin and the bottom topography, and the convergence of their roots is more complicated than for gravitational modes. A detailed discussion of the nature of the two types of modes is given by Platzman (1975) and Rao and Schwab (1976). The gravitational modes are by far the most important in the context of the diurnal and semidiurnal tides, as shown by Platzman (1984).

Table 1 gives a list of the first 20 gravitational modes in order of decreasing period. For each mode the following quantities are given: the nonrotational periods according to our model, the four

Table 1
Gravitational Modes

| Period (hr) | | | | | Energy Ratio |
| Nonrotational | | Rotational | | | (Kinetic/Potential) |
This Investigation	Platzman (F.D.)	This Investigation	Platzman (F.D.)	Platzman (F.E.)	
77.68	77.9	67.92	66.61	71.1	1.47
40.98	41.6	42.53	41.88	42.8	0.96
29.00	28.6	29.61	29.43	29.1	0.81
22.17	22.2	23.55	23.47	23.0	0.84
20.73		20.93	20.89	20.4	0.86
19.20		19.40	18.31	18.1	1.19
19.08		17.34	17.22	16.6	1.03
16.52		15.73	15.24	14.3	1.11
14.56		14.44	14.36	13.7	0.86
14.17		13.93	13.77	13.2	1.03
13.42		12.99	12.79	12.3	1.07
12.94		12.55	12.17		1.27
12.74		11.99	11.35		1.09
11.72		11.13	11.05		1.14
11.47		10.93	10.86		1.14
11.12		10.62	10.60		1.15
10.60		10.39	10.38		1.21
10.26		9.97	9.87		1.16
9.99		9.52	9.62		1.19
9.26		9.21	9.20		1.00

nonrotational periods given by Platzman (1975), the rotational periods obtained by our model, the rotational periods according to Platzman (1975) using a $6° \times 6°$ finite difference grid, and the rotational periods obtained by Platzman (1978) using a finite element grid with average area equal to that of a 4.32° equatorial square. The last entry is the ratio of energies (kinetic/potential) obtained by our model. The nonrotational gravity modes are equivalent to the eigenfunctions of the velocity potential or Proudman functions.

Table 2 lists the 20 most powerful modes for the M_2 and K_1 tidal components in order of decreasing power. The entries in the table give the power ranking, the rotational period in hours, the percentage of the total power for that mode, and the percentage of the total power contributed by all the modes included up to that point.

The three most powerful modes in the M_2 spectrum are the modes with periods of 12.99 hr (7.67%), 10.62 hr (7.33%), and 13.93 hr (7.31%). For the K_1 spectrum the three most powerful modes have periods of 23.55 hr (12.79%), 13.93 hr (8.70%), and 17.34 hr (8.19%). Figures 1 through 5 give the structure (amplitude and phase) for these five modes. The amplitudes have been normalized to a maximum value of 100, the amplitude contours are shown by the solid lines, and the dashed lines correspond to the phases.

Figures 6 and 7 show the M_2 and K_1 tidal solutions. These solutions were obtained by including the first 150 eigenfunctions from the ϕ and ψ solutions. The forced solution for η then contains 150 coefficients R_γ. The contours of equal amplitude and phase are given by the solid and dashed lines, respectively. The arrows indicate the sense of progression for high and low water.

The solution for the M_2 tide shows an amphidromic point south of Greenland and a double amphidromic system in the central North Atlantic. There is an amphidrome in the South Atlantic and several amphidromes in the periphery of the Indian Ocean; the central Indian Ocean shows the usual antiamphidromic high. The K_1 tide shows a simpler structure with amphidromic points in the central North and South Atlantic and two amphidromes in the Indian Ocean. The M_2 solution has an amplitude rms of 51.6 cm; the corresponding value for K_1 is 26 cm.

Figures 8 and 9 show the approximate location of the amphidromes for the M_2 and K_1 tidal solutions as obtained by different investigators. The results of our model are reasonable. Undoubtedly much of the variations can be attributed to poor resolution due to the coarseness of the $6° \times 6°$ grid as well as the absence of frictional effects, self-attraction, and tidal loading.

Estimation Evaluation

In the estimation of the tide we attempt to use the data wherever they are available and fit co-range and co-tidal lines to describe
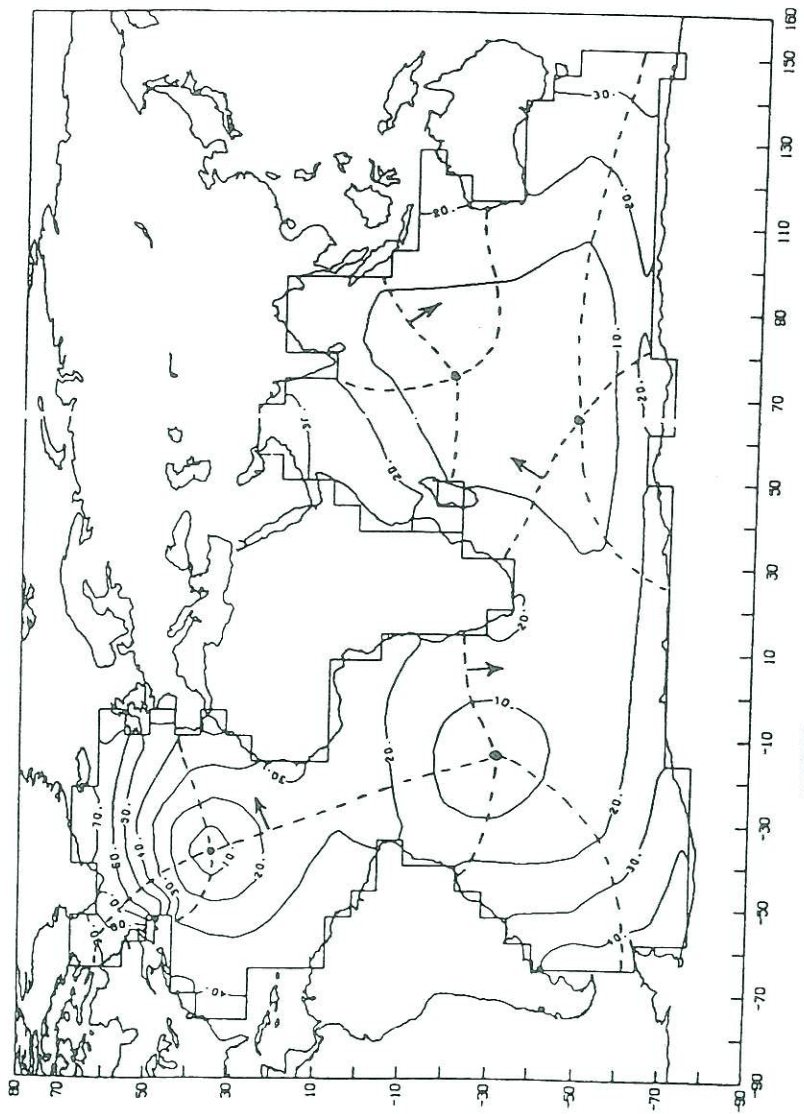
Table 2
Power Spectrum for the M_2 and K_1 Components

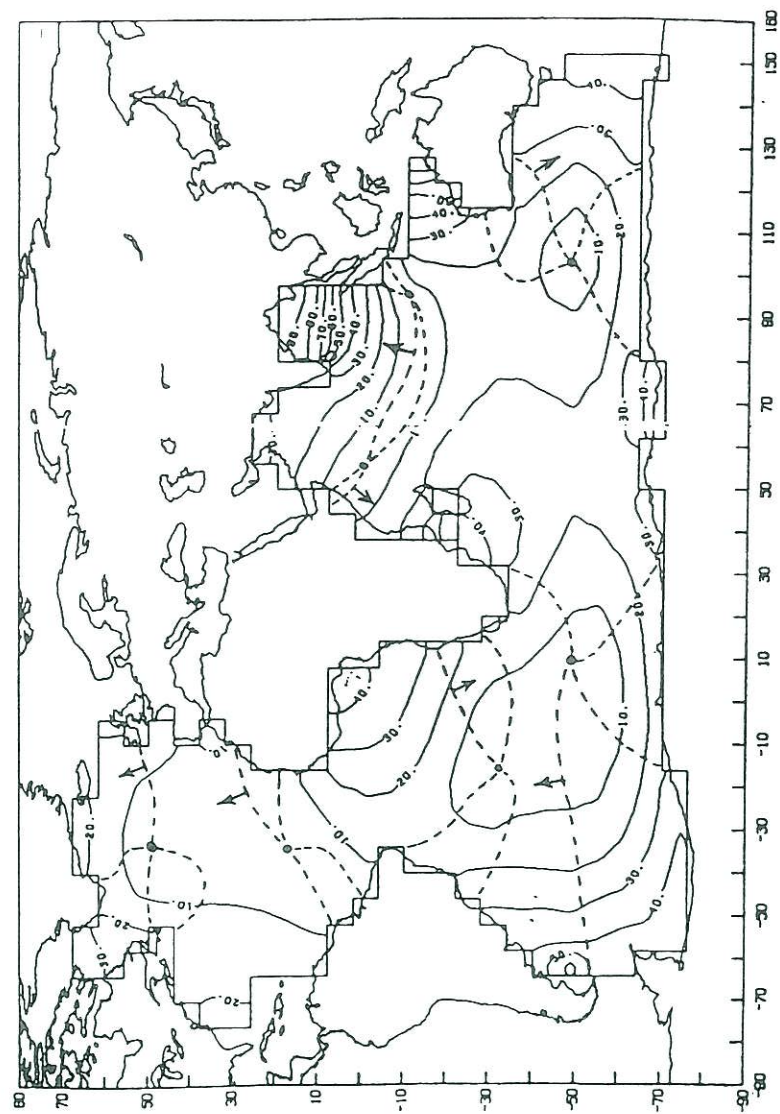| Rank	M_2			K_1		
	Period (hr)	Power (%) Each	Power (%) Sum	Period (hr)	Power (%) Each	Power (%) Sum
1	12.99	7.67	7.67	23.55	12.79	12.79
2	10.62	7.33	15.01	13.93	8.70	21.49
3	13.93	7.31	22.32	17.34	8.19	29.68
4	11.99	6.00	28.33	20.93	8.01	37.70
5	14.44	5.34	33.67	29.61	3.52	41.23
6	10.39	3.84	37.51	15.73	3.47	44.70
7	12.55	3.61	41.13	19.40	3.37	48.08
8	9.21	3.44	44.58	12.99	2.92	51.00
9	19.40	2.95	47.53	10.93	2.82	53.82
10	17.34	2.74	50.28	11.13	2.62	56.45
11	9.52	2.68	52.96	9.21	2.15	58.60
12	8.92	2.62	55.59	67.92	2.04	60.65
13	11.13	2.52	58.12	14.44	1.62	62.28
14	8.30	2.41	60.53	8.80	1.61	63.90
15	9.97	1.62	62.16	8.30	1.58	65.49
16	8.01	1.55	63.71	11.99	1.46	66.95
17	23.55	1.54	65.25	9.97	1.36	68.31
18	8.70	1.44	66.70	12.55	1.34	69.66
19	8.09	1.43	68.14	10.39	1.34	71.00
20	7.82	1.40	69.54	8.40	1.14	72.15

FIGURE 1. Normal mode, period = 23.55 hr.

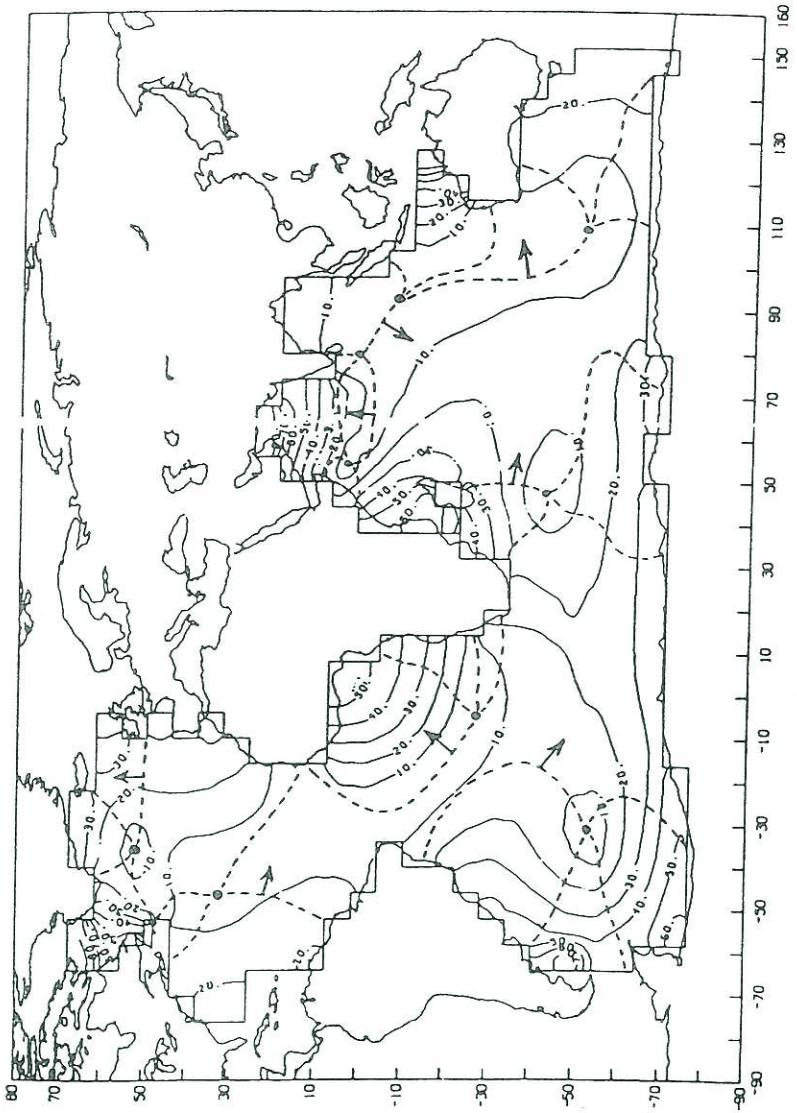**FIGURE 2.** Normal mode, period = 17.34 hr.

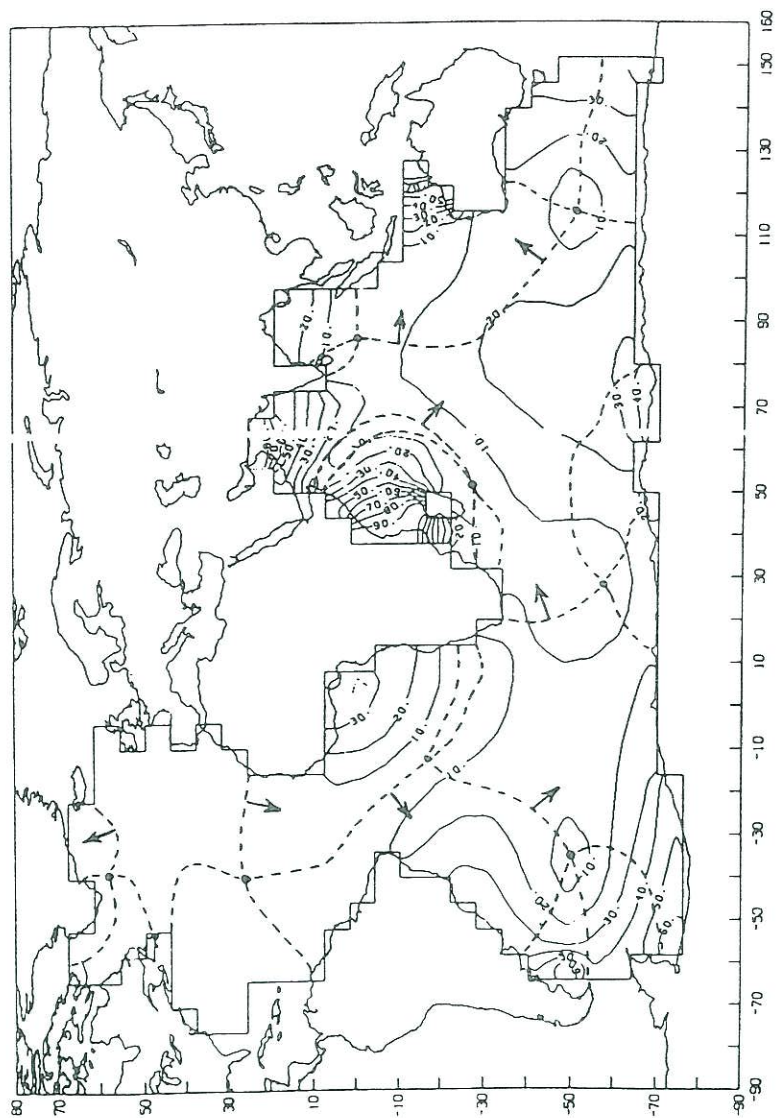FIGURE 3. Normal mode, period = 13.93 hr.
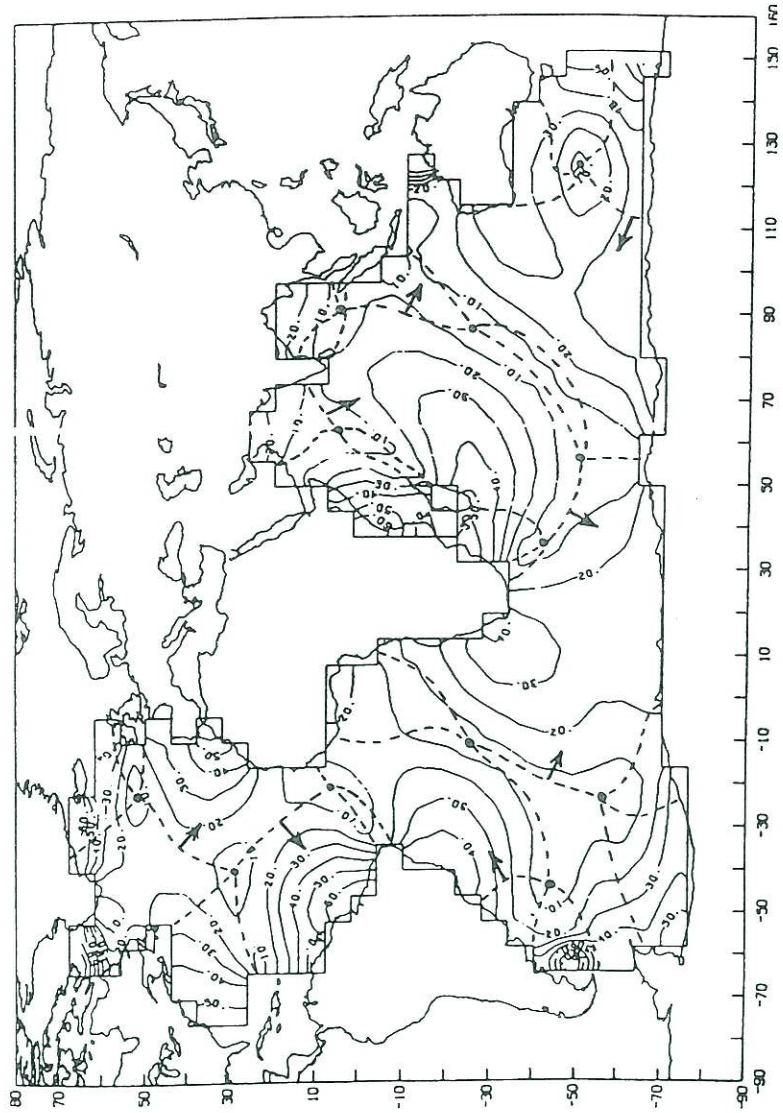

FIGURE 4. Normal mode, period = 12.99 hr.
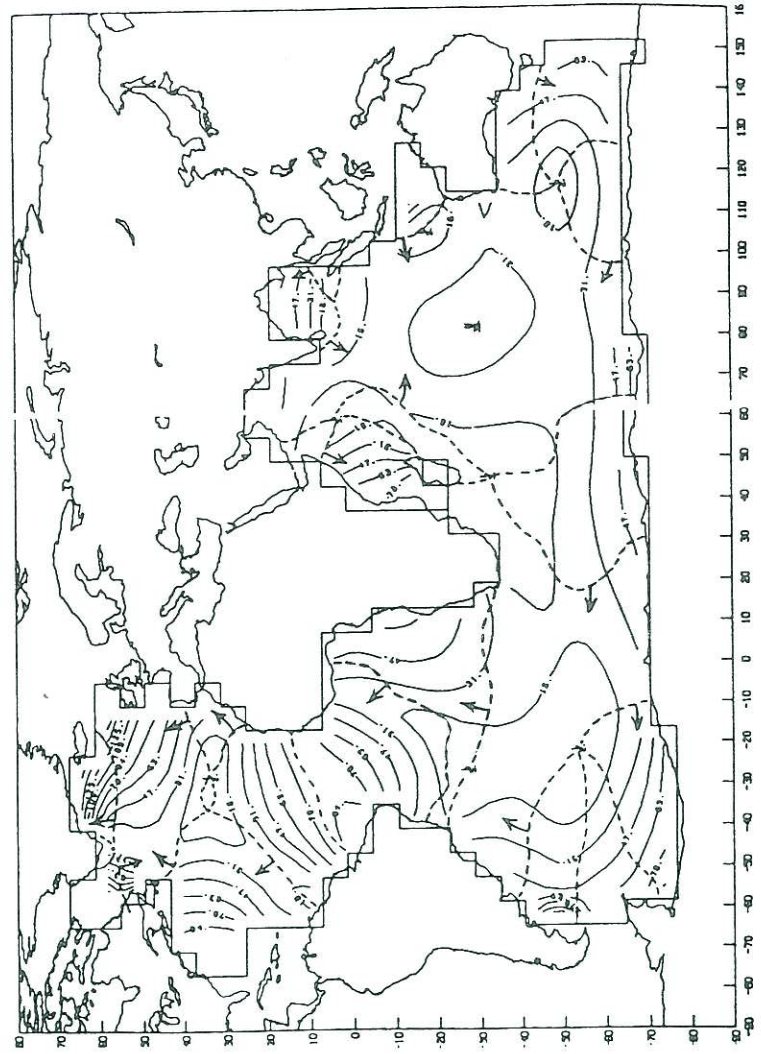
328

329

FIGURE 5. Normal mode, period = 10.62 hr.

FIGURE 6. M$_2$ tidal solution.
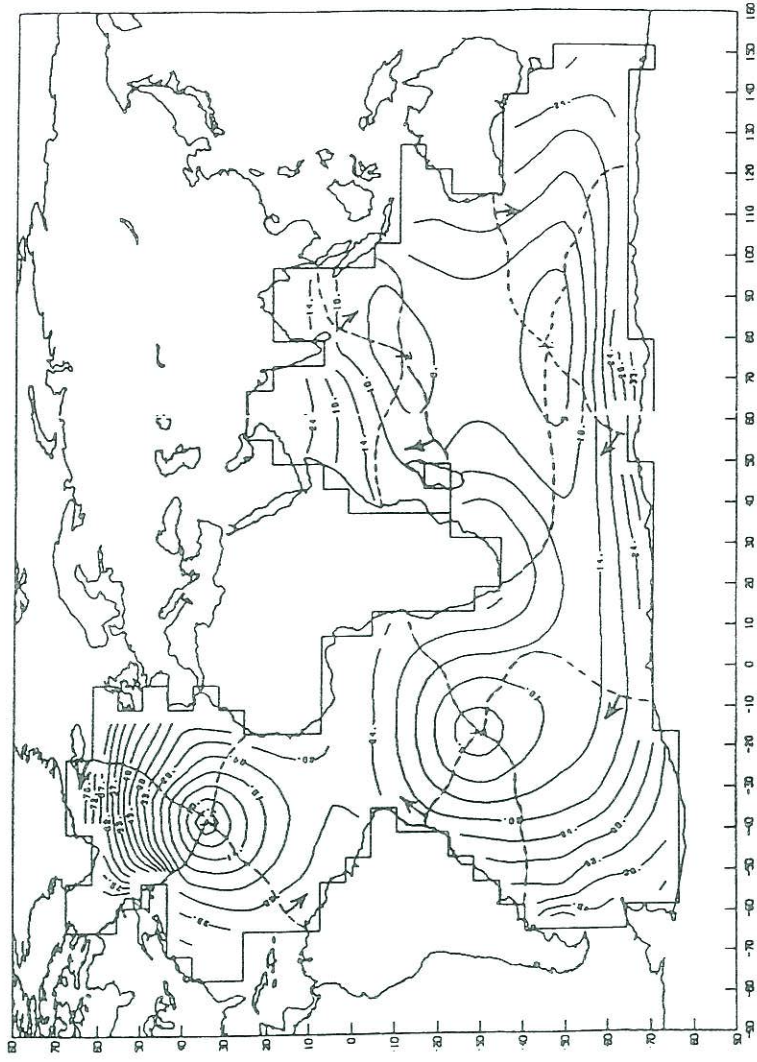
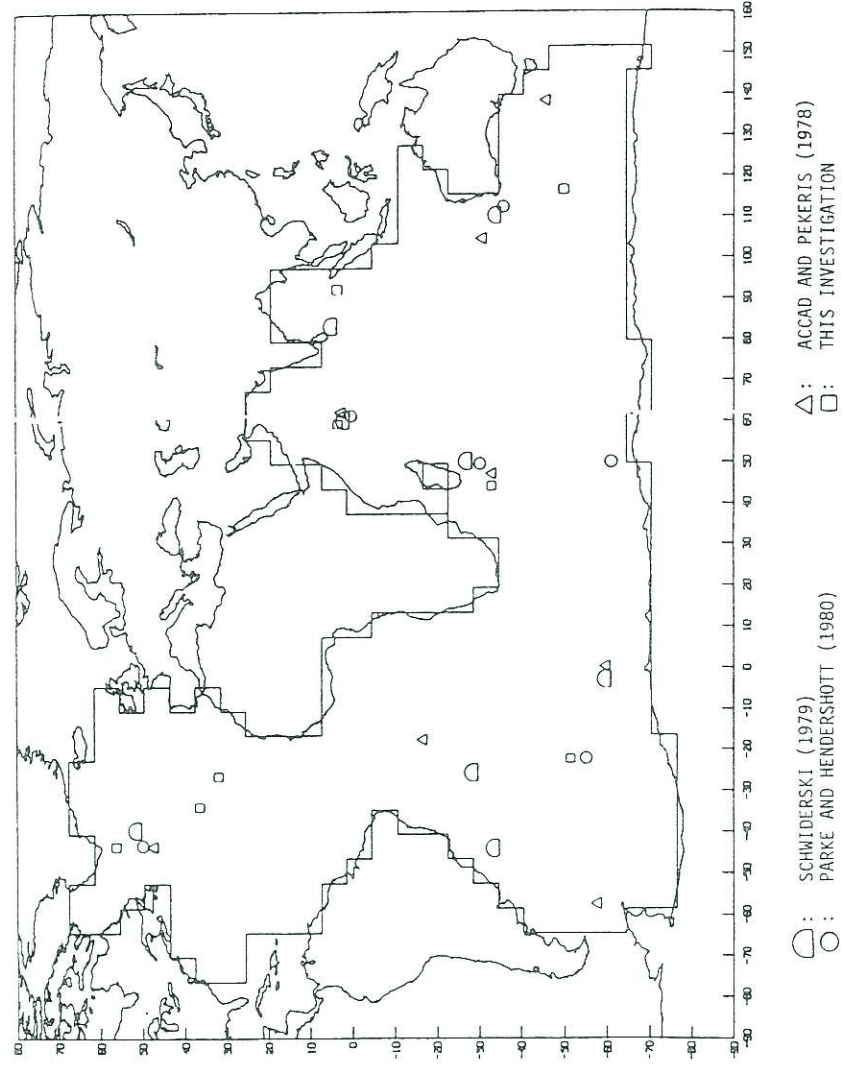FIGURE 7. K$_1$ tidal solution.

△: ACCAD AND PEKERIS (1978)
□: THIS INVESTIGATION

○: SCHWIDERSKI (1979)
○: PARKE AND HENDERSHOTT (1980)

FIGURE 8. Location of amphidromes for the M$_2$ tide.
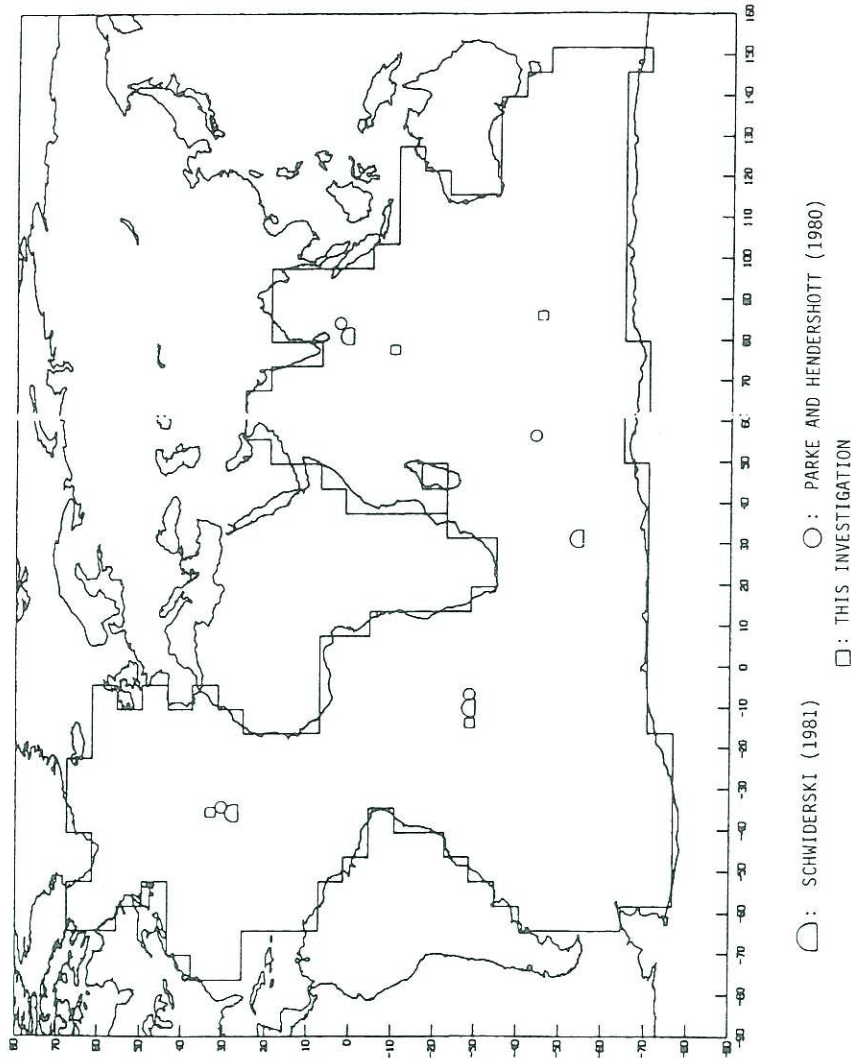
FIGURE 9. Location of amphidromes for the K_1 tide.

□ : SCHWIDERSKI (1981)   □ : THIS INVESTIGATION

○ : PARKE AND HENDERSHOTT (1980)

the tide over the entire basin using the velocity potential eigenfunctions in a least-squares sense. Since the actual tidal distribution over the entire basin is unknown, it is not possible to answer the question of how well this extrapolation procedure has worked. We have chosen to use the theoretically simulated tidal field as the "true solution" and compare the resulting tidal pattern obtained from a selected set of data points. The theoretical simulation also serves as a guide in choosing the most energetic functions to be used in the interpolation. Ideally, in the least-squares procedure it is preferable to use fewer functions than there are available data points to ensure a smooth fit and employ an *a priori* knowledge of the most dominant modes in making this selection.

To carry out testing of the estimation, two sets of data points have been created. In one case every fourth point in the ϕ field was defined as a data point, yielding the 116 data points shown in Figure 10. In the second case every sixth point was taken, to obtain the 77 data points shown in Figure 11. The tidal amplitudes and phases at these points were extracted from the theoretical simulation of the M_2 tide using 150 modes.

A comparison of the interpolated amplitudes and phases with the "true" values at all grid points is shown in Tables 3 and 4. The tables list the percentage of total grid points (462) where the analyzed and true values of amplitude and phase agree with each other within the limits indicated for the different cases corresponding to the number of modes chosen in the analysis. Also given in the table are the rms errors of the amplitude over the entire basin and only at the data points.

Tables 5 and 6 show the results obtained for the estimation of the K_1 tide. When using the data set with 116 points, the best fit to the M_2 tide is obtained when estimating the coefficients corresponding to the 58 most powerful modes; this case yields a 4.2-cm rms over the entire 462-point field. For the K_1 tide the best fit corresponds to the case when 35 coefficients are estimated, which yields a total rms of 1.9 cm. For the data set containing 77 points, the best fit to the M_2 tide is obtained when estimating the coefficients corresponding to the 32 most powerful modes, which case gives a total rms of 8.6 cm. For this data set the best fit to the K_1 tide yields a 3.3-cm total rms by estimating 34 coefficients. The
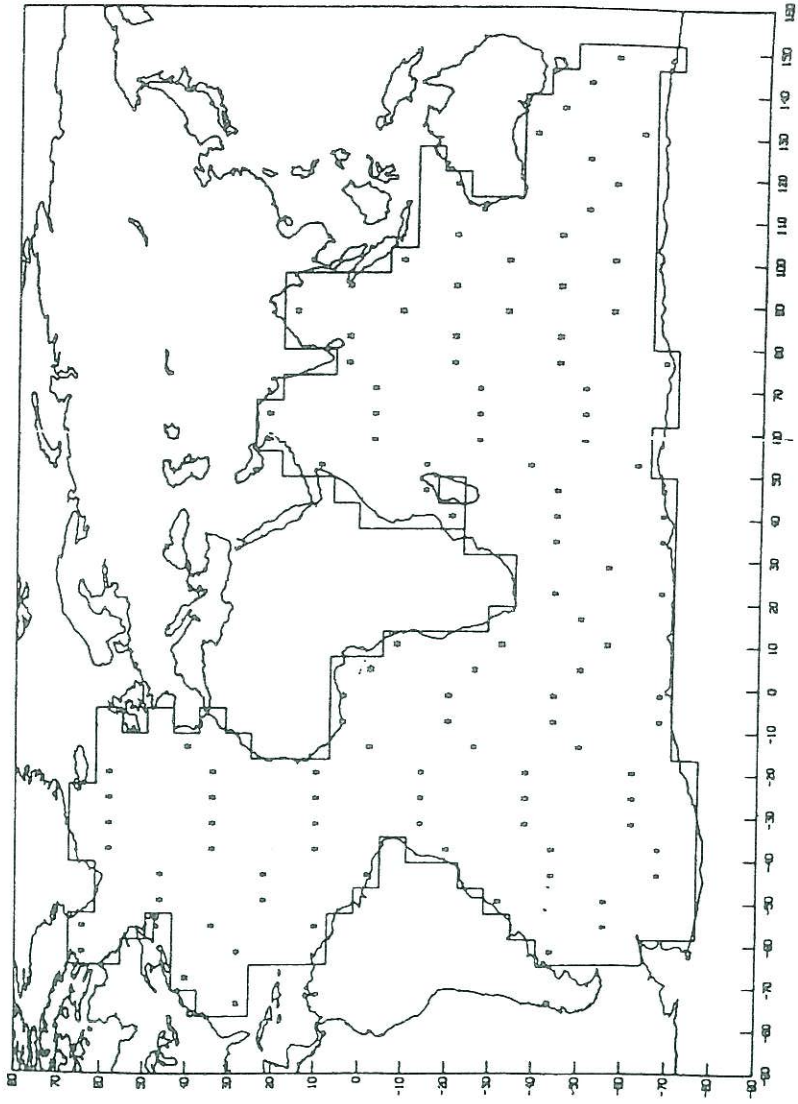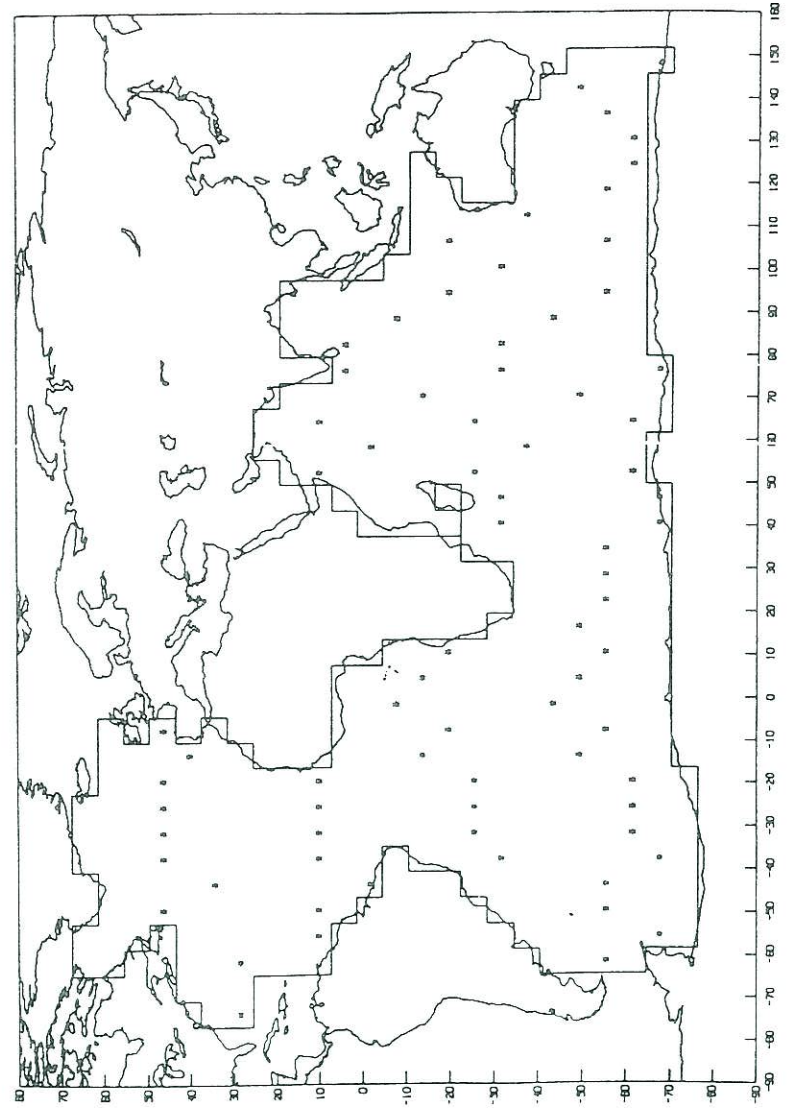
FIGURE 10. Data set (116 points).

FIGURE 11. Data set (77 points).

336

337

Table 3

Comparison between Estimated and Theoretical Fields, M_2 Component (116 Data Points)

Coefficient (% of Total Power)	Amplitude (%)			Phase (%)			Rms (cm)	
	<5%	<10%	<20%	<5°	<10°	<20°	Total	Data
14 (60.5)	14	27	48	29	48	71	11.6	9.4
29 (78.5)	35	55	79	51	75	90	5.4	3.6
39 (84.4)	37	60	83	56	78	94	7.1	2.7
48 (88.0)	47	69	88	65	84	95	7.0	2.0
58 (90.8)	53	78	92	68	87	97	4.2	1.6
68 (92.8)	56	74	89	73	84	92	9.1	0.9
80 (94.7)	58	73	88	76	89	96	19.5	0.6

Table 4

Comparison between Estimated and Theoretical Fields, M_2 Component (77 Data Points)

Coefficient (% of Total Power)	Amplitude (%)			Phase (%)			Rms (cm)	
	<5%	<10%	<20%	<5°	<10°	<20°	Total	Data
8 (44.5)	8	18	31	9	18	37	18.8	17.2
14 (60.5)	14	27	51	30	50	70	13.6	9.8
19 (68.1)	16	34	58	35	55	79	12.4	7.8
24 (74.0)	26	43	68	36	60	83	12.9	4.7
29 (78.5)	35	55	78	44	63	86	10.4	2.9
32 (80.4)	32	57	78	43	63	86	8.6	2.5
34 (81.6)	34	55	78	46	68	88	15.5	1.9
39 (84.4)	32	52	76	46	67	86	35.5	1.7

Table 5

Comparison between Estimated and Theoretical Fields, K_1 Component (116 Data Points)

Coefficient (% of Total Power)	Amplitude (%)			Phase (%)			Rms (cm)	
	<5%	<10%	<20%	<5°	<10°	<20°	Total	Data
20 (72.1)	29	48	68	43	71	94	3.4	3.2
35 (83.0)	44	69	89	69	89	97	1.9	1.2
40 (85.1)	51	73	89	73	90	97	2.1	1.0
50 (88.3)	62	81	93	73	93	99	2.2	0.8
70 (92.7)	63	84	94	78	92	97	2.2	0.3
100 (96.9)	69	81	94	79	88	96	8.1	0.07

Table 6

Comparison between Estimated and Theoretical Fields, K_1 Component (77 Data Points)

Coefficient (% of Total Power)	Amplitude (%)			Phase (%)			Rms (cm)	
	<5%	<10%	<20%	<5°	<10°	<20°	Total	Data
20 (72.1)	24	42	66	42	66	90	4.4	3.7
23 (75.3)	26	45	70	44	73	89	3.6	3.5
32 (81.6)	40	61	81	54	78	94	5.9	1.1
34 (82.6)	39	62	81	53	79	94	3.3	1.0
36 (83.5)	40	66	83	57	79	96	3.5	0.8
45 (86.8)	50	72	89	66	83	95	6.8	0.5

number of coefficients that yields the best fit is a function of the number of data points and their distribution in space in relation to the structure of the particular tidal component. Therefore, given a certain data set in the domain of an ocean basin, the theoretical simulation will help to choose the optimum number of functions to use in the interpolation. Also, by using the results of the estimation of the theoretical solution it is possible to determine the areas where additional data measurements are most needed, as shown in Figures 10 and 11. Figure 12 shows the absolute values of the differences in amplitudes between the theoretical M_2 tide using 150 coefficients and the best fit using 58 coefficients and 116 data points. Figure 13 shows the corresponding values for the K_1 tide when using a best fit of 35 coefficients. To facilitate display, the numbers are rounded to the nearest digit. In the M_2 case there are areas in the northeast Atlantic with higher than average rms. The highest discrepancies occur at some isolated points off the coast of Labrador, Greenland, northern Australia, and east Antarctica. The K_1 fit shows some high values in the northeast Atlantic and the Patagonian shelf as well as in the Antarctic area in the Indian Ocean.

We shall point out that we have not tested every possible combination of modes when estimating the coefficients to fit the tide in the different cases. An exhaustive search might yield still better results for the Proudman functions.

Modeling Errors in the Data

The altimetric measurements provided by satellites are not free of errors and any method that uses the data will be affected by them. A detailed discussion of these errors in the context of tidal extraction is given by Estes (1980) and Woodworth and Cartwright (1986), among others. To ascertain what the effects of these errors might be in the context of our technique, we introduce some simple models for the error distribution. These models are not intended to reproduce exactly the real errors found in real data, but hopefully they are representative of worst-case situations and will shed some light on what to expect in the real case. First we divide the Atlantic-Indian basin into three different regions, corresponding to the
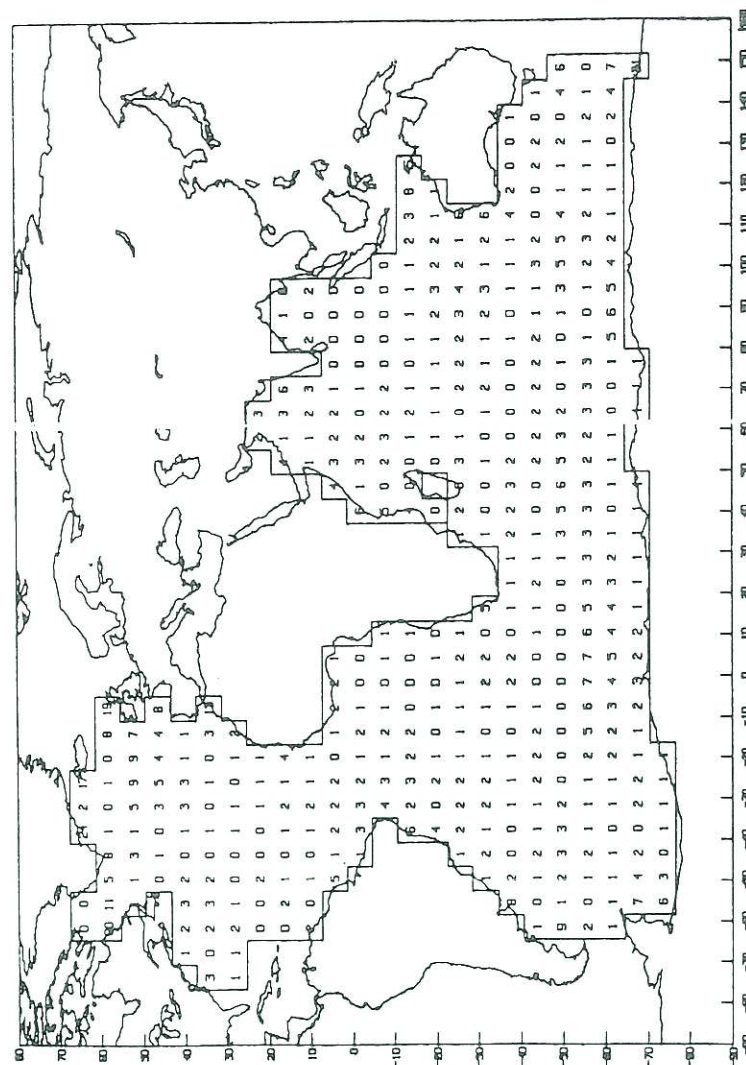

FIGURE 12. M_2 tide: amplitude differences (cm) between theoretical solution using 150 coefficients and 58 coefficient solution from 116-point data set.

FIGURE 13. K_1 tide: amplitude differences (cm) between theoretical solution using 150 coefficients and 35 coefficient solution from 116-point data set.

Atlantic, Indian, and East Indian Oceans, as shown in Figure 14. Three error models will be tested:

1. The first model will be a 10-cm error in the amplitude of the tide throughout the entire basin.
2. The second model introduces a 20-cm error in the tidal amplitude throughout the entire Indian Ocean (including the East Indian).
3. The third model consists of a 40-cm error in the tidal amplitude of the East Indian basin only.

In each case the error is assumed to be a positive additive constant with no random component.

First we test a data set consisting of the 462 points where our theoretical solution is defined; the results are given in Table 7. The behavior of the solution is linear and stable. There is, of course, a propagation of error, and the quality of the results in the immediate area of the data is only as good as the data itself. The inclusion of more Proudman functions in the estimation does not produce better results in all cases. Table 8 gives the results for the 116-point data set; the behavior is similar but now there are two sources of error: the data errors and the errors due to the estimation procedure. They seem to behave in an additive manner. However, when no data errors were present the solution with 58 functions gave better results than the 29-function solution. As shown in Table 3, the rms values for the entire basin were 4.2 cm and 5.4 cm, respectively. For the three error models tested the 29-function solution gives better results, which indicates that any pre-solution analysis should include some sort of error modeling, the more realistic the better.

Fitting Mazzega's M_2 with Proudman Functions

Mazzega (1985) used the SEASAT data to obtain a spherical harmonic expansion for the M_2 tide in the world oceans, this was the first attempt to estimate the deep ocean tides from satellite altimeter data, Woodworth and Cartwright (1986) discuss Mazzega's method to some extent. We have used Mazzega's spherical harmonics coefficients to create values of amplitude and phase for the M_2 tide at the 462 points of our grid. We have used his expansion to degree
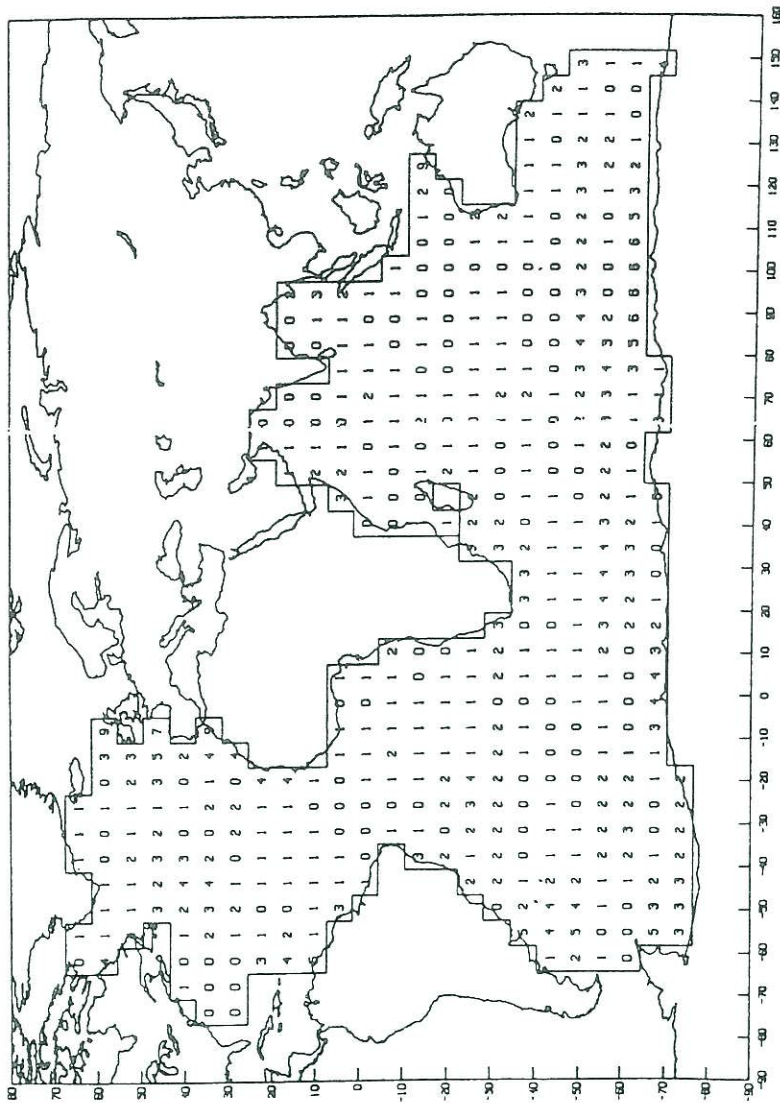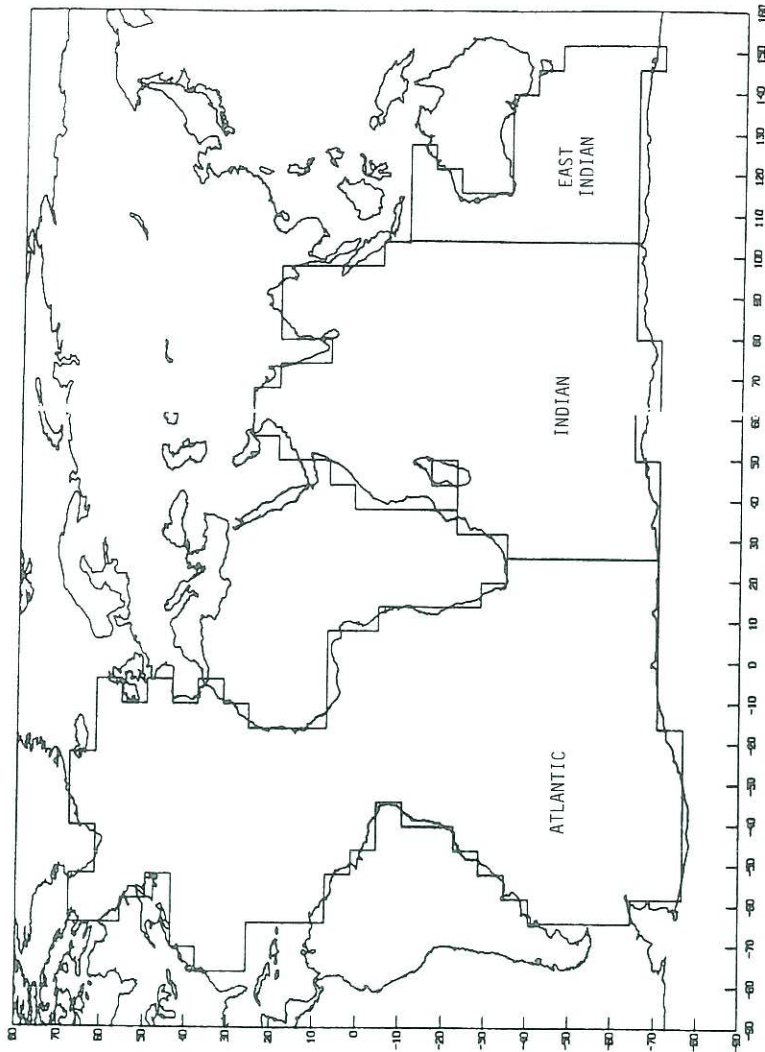
FIGURE 14. Regions used in modeling data errors.

Table 7
Fitting M$_2$ with Proudman Functions, 462 Data Points,
Errors Included

		Rms (cm)			
Error	Function	Entire Basin	Atlantic	Indian	East Indian
	29	9.5	9.4	9.6	8.1
10 cm	58	9.4	9.4	9.4	9.4
entire	100	9.6	9.6	9.6	9.3
basin	150	9.7	9.8	9.7	9.6
	29	11.9	4.9	16.8	17.1
20 cm	58	12.2	3.3	17.6	18.8
Indian	100	12.7	2.7	18.5	18.8
Ocean	150	13.0	2.0	19.0	19.5
	29	10.1	4.7	14.1	23.7
40 cm	58	10.9	2.7	15.8	30.8
East	100	11.5	1.6	16.9	34.5
Indian	150	12.1	0.5	17.9	36.8

and order 6, which yields his best model. This is not intended to represent a better alternative to a fit to the actual data, as Woodworth and Cartwright (1986) have done. We would like to pursue such an approach in the future using Proudman functions computed with a finer resolution than our present 6° × 6° grid allows.

Table 8
Fitting M$_2$ with Proudman Functions, 116 Data Points,
Errors Included

		Rms (cm)			
Error	Function	Entire Basin	Atlantic	Indian	East Indian
10 cm	29	12.1	12.6	11.5	14.5
entire basin	58	13.7	15.4	11.3	15.4
20 cm	29	15.0	5.7	21.2	29.8
Indian Ocean	58	21.5	12.4	28.7	48.9
40 cm	29	12.6	6.7	17.1	30.7
East Indian	58	16.7	11.0	21.6	42.0

Table 9
Fitting Mazzega's M_2 (Spherical Harmonic
Expansion to Degree and Order 6) with
Proudman Functions

Function	Rms (cm)		
	Entire Basin	Atlantic	Indian
29	12.0	12.0	12.0
58	9.2	10.8	6.9
68	7.9	9.0	6.3
80	5.1	4.9	5.3
100	4.4	4.5	4.3
150	4.1	4.2	4.0
200	3.9	4.0	3.9

However, Mazzega's solution reproduces many of the features predicted by numerical models such as Schwiderski's (1979); therefore, a fit to his solution using Proudman functions should be of some interest. The results are given in Table 9. We find that the fit gets progressively better as we increase the number of functions, although the rate of improvement slows down considerably after the first 100. We did not try more than 200 functions, at which point the fit was down at the 4-cm level. The rms in sea surface height difference between our theoretical solution (150 modes) and Mazzega's was 27.36 cm before the fit.

Conclusions

A method has been developed to interpolate tidal data to map the tidal components over an entire basin. The technique has been demonstrated in an application to the Lake Superior basin by Sanchez et al. (1985). Now it has been applied to the Atlantic-Indian ocean basin using a $6° \times 6°$ finite difference grid.

The computed normal modes agree fairly well with those obtained by Platzman (1975) using a different approach. The forced solutions for the M_2 and K_1 tidal constituents were computed also. These theoretical simulations show the same general pattern obtained by other modelers (i.e., Platzman, 1984; Schwiderski, 1983; Parke and Hendershott, 1980; Accad and Pekeris, 1978). The theoretical so-

lutions were obtained by including 150 eigenfunctions of the velocity potential. The resulting height and phase fields were used as data to test the estimation technique and as a guide in choosing the most energetic functions. The results of the interpolation show that it is possible to recover the M_2 and K_1 components with a degree of accuracy well within the error bounds of present satellite techniques.

In the light of the recent investigation by Woodworth and Cartwright (1986) in which they used the normal modes obtained by Platzman as basis functions for the interpolation, a few observations might be pertinent. We believe the adoption of the Proudman functions as a basis offers the advantage of simplicity since to compute these functions it is only necessary to solve the first of equations (7). It is possible to perform accuracy tests on a real data set. A certain amount of knowledge as to the magnitude and geographic distribution of the errors in the data is probably important in this last context. The Proudman functions also offer the advantage of being free of the dynamic prejudice introduced by factors such as friction. The choice between finite differences and finite elements in the numerical computation of the solution deserves some attention. Finite differences are probably easier to implement in terms of the initial effort required, while finite elements are probably better suited to the modeling of irregular boundaries. In either case the increasing power of the last-generation computers should allow the adoption of finer grids with better resolution.

Future applications of the method should consider its extension to the Pacific basin, the adoption of a grid with finer resolution, the incorporation of real data from gauges and satellite measurements, and the simulation and analysis of other tidal constituents. The method is especially suited for the latter since the eigenfunctions of the velocity potential (Proudman functions) of a particular basin are dependent only on its shape and depth, and they have to be computed only once.

References

Accad, Y., and C. L. Pekeris. 1978. Solution of the tidal equations for the M_2 and S_2 tides in the world oceans from a knowledge of the tidal potential alone. *Philos. Trans. R. Soc. London* 290.

Cartwright, D. E. 1977. Oceanic tides. *Rep. Prog. Phys.* 40.

Estes, R. H. 1980. A simulation of global ocean tide recovery using altimeter data with systematic orbit error. *Mar. Geod.* 3(1–4).

Hendershott, M. C., and W. H. Munk. 1970. Tides. *Annu. Rev. Fluid Mech.* 2.

Hendershott, M. C. 1973. Ocean tides. *EOS* 54(2).

Hendershott, M. C. 1977. Numerical models of ocean tides, in E. D. Goldberg et al., eds., *The Sea*, Vol. 6: *Marine Modeling*. New York: Wiley–Interscience.

Hendershott, M. C. 1981. Long waves and ocean tides, in *Evolution of Physical Oceanography*. Cambridge, Mass.: The MIT Press.

Mazzega, P. 1985. M2 model of the global ocean tide derived from SEASAT altimetry. *Mar. Geod.* 9.

Parke, M. E., and M. C. Hendershott. 1980. M_2, S_2, K_1 models of the global ocean tide on an elastic earth. *Mar. Geod.* 3(1–4).

Platzman, G. W. 1975. Normal modes of the Atlantic and Indian Oceans. *J. Phys. Oceanogr.* 5.

Platzman, G. W. 1978. Normal modes of the world ocean: I. Design of a finite-element barotropic model. *J. Phys. Oceanogr.* 8.

Platzman, G. W. 1981. Normal modes of the world ocean: II. Description of modes in the period range 8 to 80 hours. *J. Phys. Oceanogr.* 11.

Platzman, G. W. 1984. Normal modes of the world ocean: IV. Synthesis of diurnal and semidiurnal tides. *J. Phys. Oceanogr.* 14.

Proudman, J. 1918. On the dynamical equations of the tides. *Proc. London Math. Soc.* 18.

Rao, D. B. 1966. Free gravitational oscillations in rotating rectangular basins. *J. Fluid Mech.* 25.

Rao, D. B., and D. J. Schwab. 1976. Two-dimensional normal modes in arbitrary enclosed basins on a rotating earth: application to Lakes Ontario and Superior. *Philos. Trans. R. Soc. London, Ser. A* 281.

Rao, D. B., and D. J. Schwab. 1981. A method of objective analysis for currents in a lake with application to Lake Ontario. *J. Phys. Oceanogr.* 11.

Sanchez, B. V., D. B. Rao, and P. G. Wolfson. 1985. Objective analysis for tides in a closed basin. *Mar. Geod.* 9.

Schwiderski, E. W. 1979. Global ocean tides: II. The semidiurnal principal lunar tide (M2), Atlas of tidal charts and maps. NSWC TR 79-414.

Schwiderski, E. W. 1980. Ocean tides: I. Global ocean tidal equations; Ocean tides: II: A hydrodynamical interpolation model. *Mar. Geod.* 3(1–4).

Schwiderski, E. W. 1981. Global ocean tides: IV. The diurnal luni-solar declination tide (K1), Atlas of tidal charts and maps. NSWC TR 81-142.

Woodworth, P. L., and D. E. Cartwright. 1986. Extraction of the M2 ocean tide from SEASAT altimeter data. *Geophys. J. R. Astr. Soc.* 84.